Modeling of MARSIS Segmented Booms and Prediction of In-Flight Dynamics of the Mars Express Spacecraft*

Edward Mettler[†] and Marco Quadrelli

August 26, 2002

Abstract

In this paper we provide an independent modeling and dynamic analysis of the MARSIS Antenna segmented booms deployed on the Mars Express Spacecraft. The Mars Express Mission is a joint NASA/ESA Cooperative project. The Mars Express Spacecraft being built by ESA will be launched in June 2003 and arrive at Mars in December 2003 to begin a four year study of the planet's atmosphere, surface, and subsurface. The Mars Advanced Radar for Subsurface and Ionospheric Mapping (MARSIS), provided by NASA and managed by JPL, is a key instrument in the search for water on Mars. Our objective was to determine the antenna's dynamic interaction with the spacecraft bus (or central rigid body). Static and modal analyses make use of boom material parameters, mass properties, and laboratory test results provided by TRW Astro Aerospace, Goleta,CA, in addition to data on spacecraft mass properties and orbital parameters from Astrium, Toulouse, France. Solutions are derived involving coupled equations of motion for vehicle orbital mechanics, rigid body spacecraft bus, and flexible-appendages dynamics. Numerical simulations were performed of a "flying model" of the spacecraft in the perigee phase of its elliptical Mars orbit, with all MARSIS booms fully deployed and Reaction Wheels used to both disturb and control the spacecraft attitude. The spacecraft's Reaction Wheel model and Attitude Controller were designed by the authors and is not optimized nor based on any specific information provided by Astrium. Realistic excitations of the bus and boom appendages were imposed by short reaction wheel torque-time profiles that were constructed to maximize excitation of the system fundamental vibration mode. To clearly identify only the MARSIS interaction with the bus, the solar panels were modeled as rigid elements, and the attitude sensors and reaction wheels were assumed to be free from noise and other errors. The simulation results verify the Antenna system modeling fidelity and provide data on proximate "worst case" dynamic interactions between the flexible booms and the spacecraft bus that demonstrate the MARSIS dynamic compatibility with the spacecraft.

1 INTRODUCTION

This paper provides an independent modeling and dynamic analysis of the MARSIS Antenna segmented booms deployed on the Mars Express Spacecraft. This work was done on behalf of the

---

*Copyright © 2002 by the American Institute of Aeronautics and Astronautics, Inc. The U.S. Government has a royalty-free license to exercise all rights under the copyright claimed herein for Governmental purposes. All other rights are reserved by the copyright owner.

[†] Mail Stop 198-138, Jet Propulsion Laboratory, California Institute of Technology, Pasadena, CA 91109-8099, edward.metter@jpl.nasa.gov

JPL MARSIS Experiment Project Office to establish the highest confidence for the Antenna System in-flight dynamics compatibility with the Mars Express mission ([1], [2], [4]).

The Mars Express Mission is a joint NASA/ESA Cooperative project. The Mars Express Spacecraft being built by ESA will study Mars for about four years from a highly elliptical orbit (15,000 km apoapsis and 250 km periapsis altitude) with seven major science instruments on the spacecraft plus a small lander vehicle, named Beagle 2. The mission will be launched about June 2003 and arrive at Mars in December 2003. The Mars Advanced Radar for Subsurface and Ionospheric Mapping (MARSIS), provided by NASA and managed by JPL, is a key instrument in the search for water on Mars. It is a four frequency band Synthetic Aperture Altimeter with penetration capability for subsurface and atmospheric sounding from 40 meter long dipole antennas oriented parallel to the planet surface and a 7 meter long monopole along the nadir for clutter cancellation.

Our objective was to determine the antenna's dynamic interaction with the spacecraft bus (or central rigid body). Static and modal analyses make use of boom material parameters, mass properties, and laboratory test results provided by TRW, in addition to Astrium data on spacecraft mass properties and orbital parameters. Solutions are derived involving coupled equations of motion for vehicle orbital mechanics, rigid body spacecraft bus, and flexible-appendages dynamics. Numerical simulations were performed of a "flying model" of the spacecraft in the perigee phase of its elliptical Mars orbit, with all MARSIS booms fully deployed and Reaction Wheels used to both disturb and control the spacecraft attitude. The spacecraft's Reaction Wheel model and Attitude Controller were designed by the authors and is not optimized nor based on any specific information provided by Astrium. Realistic excitations of the bus and boom appendages were imposed by short reaction wheel torque-time profiles that were constructed to maximize excitation of the system fundamental vibration mode. To clearly identify only the MARSIS interaction with the bus, the solar panels were modeled as rigid elements, and the attitude sensors and reaction wheels were assumed to be free from noise and other errors. The simulation results verify the Antenna system modeling fidelity and provide data on proximate "worst case" dynamic interactions between the flexible booms and the spacecraft bus that demonstrate the MARSIS dynamic compatibility with the spacecraft.

1.1 Approach to the Dynamic Analysis and Modeling

Clearly, the MARSIS uniquely segmented booms present a dynamic modeling challenge and a special problem in predicting the on-orbit deployed dynamic behavior. For the Mars Express mission, where a precise attitude pointing stability prediction is required, the solution needs to include the segmented dipole and monopole antennas flexible boom appendages, the attachment boundary conditions, and the rigid body inertial dynamics of the spacecraft in its Martian elliptical orbit with orbital mechanics, gravity gradient torques, and closed-loop reaction wheel control. The following modeling, analysis, and simulations were performed with this approach.

From Figures 1 and 2 we observe that, in the deployed state, the appendage model is far from being a uniform, homogeneous beam. Rather, it consists of 13 segments hinged together by some kinematic constraints. This motivates the multi-body analysis to be discussed next.

1.2 Assumptions of the Dynamic Model

A dynamic model of the deployed dipole and monopole booms was derived with the following assumptions:

- Only a small portion of the orbit is simulated, i.e., 100 seconds representing the spacecraft's periapsis passage in its elliptical Mars orbit.

- The spacecraft bus is modeled as a rigid body with three Reaction Wheels aligned along the principal axes.
- The spacecraft Attitude Control System is deliberately modeled with perfect position and rate reference sensors. Reaction Wheels are modeled with realistic rotor inertia, momentum storage, and torque capabilities.
- The solar panels are deliberately modeled as rigid fixed elements, and their inertia contribution is included in the moment of inertia matrix of the bus about its center of mass. This is done to avoid additional complications in the model, but primarily because the solar panels are much more stiff than the antennas.
- The vehicle dynamics is coupled to the orbital dynamics, but the spacecraft undergoes only small rotational motions of less than one degree.
- The monopole and dipole booms were first modeled as cantilever beams of uniform and homogeneous material properties along their length. However, we were **not able to come close** to the experimental results provided by TRW.
- An improved equivalent model was derived assuming that each boom is modeled as a serial chain of hinged flexible beams, with rotational springs at the "root" (attachment point to the bus) and between the segments.
- The root spring constants are obtained from the TRW static deflection water tank (zero-g) tests
- The rotational spring constants between each hinged segment are kept as free parameters in order to match the first mode of the tested article. The hinges are modeled as perfect spherical joints.

1.3 Boom-Bus Attachment Boundary Condition Influence

Comparative information is presented below that shows the dynamic behavior that supports the conservatism of using fixed - free, or various degrees of fixity such as "root" hinge stiffness, versus the actual in-space condition of quasi free - free boundaries seen by the MARSIS booms. The term "quasi" is used to express that the spacecraft central body mass and rotational inertia will impose force and moment constraints on the boom root interface. If the central body were massless then a true free - free boundary condition would be present for the booms.

The following approximate functional relationship from Ref. ([3]) provides an insight into Boundary Condition influence on the natural frequencies (in [rad/s]) of homogeneous cantilever beams :

$$f_j = \frac{a_j^2}{L^2}\left(\frac{EI}{m}\right)^{\frac{1}{2}} \tag{1}$$

where: j = 1, 2, 3, ...n; a_j = Non-rigid body mode coefficients (iteratively derived from transcendental hyperbolic equations for homogeneous cantilever beams); L = length of beam; E = modulus of elasticity; I = area moment of inertia of beam about neutral axis; m = mass per unit length of beam.

Then, comparing the two extreme cantilever beam boundary conditions of **Fixed-Free vs Free-Free**, the first four mode coefficients, a_j, are:

Non-Rigid Body Mode Number	Fixed (or Clamped) - Free	Free - Free
1	1.8751	4.7300
2	4.6941	7.8532
3	7.8547	10.9956
4	10.9955	14.1371

One can readily see the ratio of the a_j^2 terms for two boundary conditions provides modal frequency scaling, e.g., the first modes will have $(4.7300)^2$ / $(1.8751)^2 = 6.364/ 1$. Thus the pure free - free beam fundamental frequency will be 6.364 times higher than the fixed - free beam fundamental frequency.

While these facts provide a conservative direction for TRW's results, **they do not allow accurate prediction** of the actual in-flight dynamics of the segmented MARSIS booms. It is clear, however, that the finite stiffness of the "root" hinge is **not a fixed** or clamped case, and *tends towards a free-free* case or higher frequency. Mitigating that are the segment "spliced-joints" which tend to lower the overall boom stiffness. Prediction of the resulting global dynamics of the booms requires much further modeling and analysis, and makes careful use of the TRW test results.

1.4 Boom Stiffness Symmetry

TRW conducted static load-deflection water tank (~zero-g) tests of the fully deployed 20-meter boom to determine the global bending transverse stiffness, the stiffness of the boom "root" in the two transverse directions, K_{ry} and K_{rz}, and also to obtain data on the stiffness of the "spliced" joints. The x direction is defined as the roll axis (see Figure 1), whereas the y and z axes are the yaw and pitch axes respectively.

The "root" stiffness K_{ry} was found to be 926.47 N-m/radian (or 8200 in-lb/rad), and K_{rz} was 206.76 N-m/radian (or 1830 in-lb/rad). Thus, the "root" section was 4.48 times stiffer in the K_{ry} direction. This is not surprising since the slotting of the boom tube at the segment fold points creates an obvious asymmetry.

The test data also indicated the stiffness of the typical "spliced" section was 2.6 times greater in the z direction then the y direction. This result is opposite to the "root" stiffness asymmetry, and leads to the expectation that the combined segmented boom deflections due to "root and splices" will tend to cancel out local differences in directionality for the global boom behavior.

These static deflection tests also indicated reasonable transverse symmetry for the global stiffness, that was later confirmed by the symmetric frequencies obtained from the TRW **ten-meter Free-Fixed** boom scaled impulse response dynamic tests. We have therefore taken this into account in this analysis and detailed modeling of the segments and joints, and assumed approximately the same **global** stiffness and natural frequencies in both transverse directions of the fully deployed booms.

2 EQUATIONS OF MOTION

The equations of motion of the entire system will be derived in this section. An inertial reference fram $\mathcal{F}_I$ is defined by the X-axis along the vernal equinox, the Z-axis along the direction of the system's angular momentum, and the Y-axis completes the right-handed triad. The origin of $\mathcal{F}_I$ is placed at the center of a Mars geocentric frame. The position and velocity of the center of mass of bodies i and j (also representing nodes i and j of an extended finite element body) is given by vectors $\mathbf{r}_i$ and $\mathbf{r}_j$, and $\dot{\mathbf{r}}_i$ and $\dot{\mathbf{r}}_j$ respectively measured from the origin of $\mathcal{F}_I$. Similarly, the attitude of the reference frames $\mathcal{F}_i$ and $\mathcal{F}_j$ of bodies i and j with respect to the inertial frame $\mathcal{F}_I$ is described by

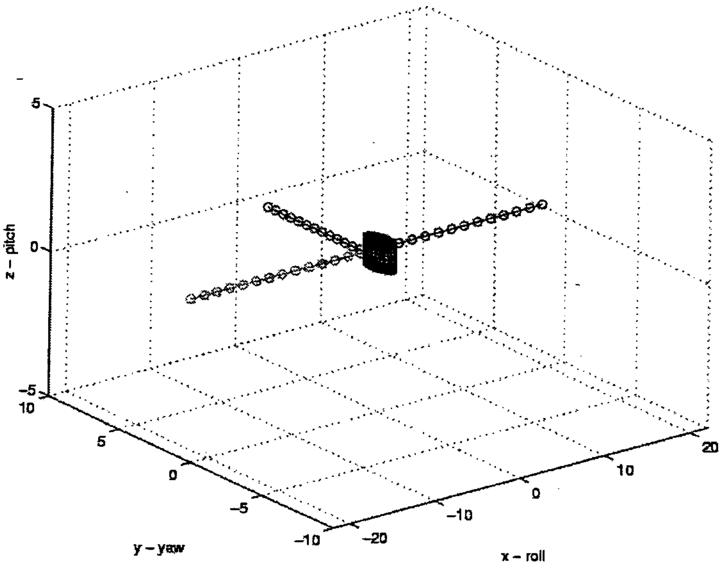
5
0
-5
z - pitch
10
5
0
-5
-10
y - yaw
-20
-10
0
10
20
x - roll

Figure 1: Finite element model of vehicle with deployed MARSIS antennas.

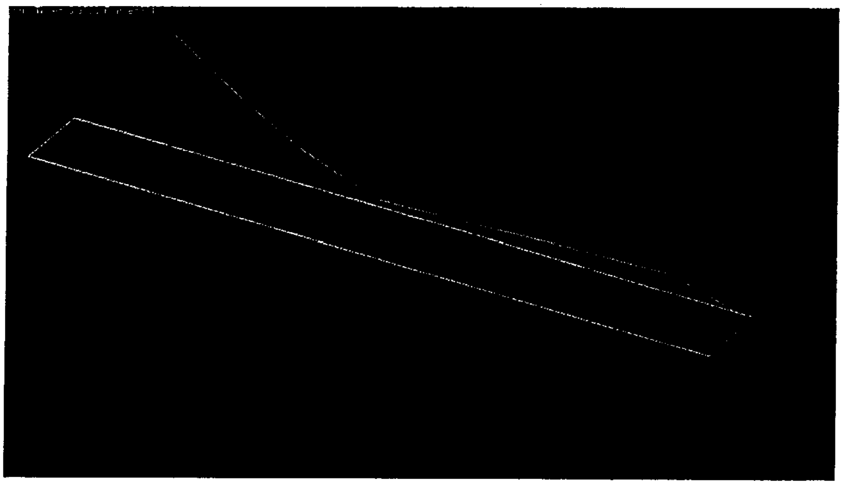

Figure 2: Dipole Boom Deployment in Vacuo.

tensors $\mathbf{A}_i$ and $\mathbf{A}_j$, and their angular velocity by vectors ω_i and ω_j, respectively. We parameterize the translation of body i by the components of vectors $\mathbf{r}_i$ and $\dot{\mathbf{r}}_i$ in $\mathcal{F}_I$, and its rotation wrt. $\mathcal{F}_I$ by the quaternion parameters $\mathbf{q}_i$ and the angular velocity ω_i. It is also useful to introduce the orbiting reference frame $\mathcal{F}_{ORF}$, which we use to describe the near field dynamics of the spacecraft relative to its orbit. This reference frame is attached to a point that follows a Keplerian orbit around the primary body. $\mathcal{F}_{ORF}$ is defined by the direction of the orbital velocity vector (x-axis), the local vertical (z-axis), and the orbit normal (y-axis). The orbit of the origin of $\mathcal{F}_{ORF}$ is defined by the six orbital elements a (semimajor axis), e (eccentricity), i (inclination), Ω_l (longitude of ascending node), ϖ (argument of perigee), ν (true anomaly), and time of passage through perigee. The orbital radius is R_0, and the orbital angular velocity vector is denoted by $\nleq$.The transformation between $\mathcal{F}_{ORF}$ and $\mathcal{F}_I$ is given by $\mathcal{F}_{ORF} = \mathbf{R}\mathcal{F}_I$ with

$$\mathbf{R} = \begin{bmatrix} 1 & 0 & 0 \\ 0 & -1 & 0 \\ 0 & 0 & -1 \end{bmatrix} \mathbf{R}_3\left(\varpi + \nu\right)\mathbf{R}_2\left(i\right)\mathbf{R}_3\left(\Omega_l\right) \tag{2}$$

where $\mathbf{R}_i\left(\cdot\right)$ denotes a rotation matrix of $(\cdot)$ around the direction specified by the subscript. It is useful to refer the translational dynamics of body i to the origin of $\mathcal{F}_{ORF}$. Therefore, we have

$$\mathbf{r}_i = \mathbf{R}_0 + \boldsymbol{\rho}_i \tag{3}$$

We define the state vector as:

$$\begin{aligned} \mathbf{X} \;\; = \;\; & (\mathbf{R}_0, \boldsymbol{\rho}, \mathbf{q}, \sigma_1, \sigma_2, \sigma_3, \boldsymbol{\rho}_1, \boldsymbol{\theta}_1, ..., \boldsymbol{\rho}_\mathrm{N}, \boldsymbol{\theta}_N, \\ & \dot{\mathbf{R}}_0, \dot{\boldsymbol{\rho}}, \omega, \Omega_1, \Omega_2, \Omega_3, \dot{\boldsymbol{\rho}}_1, \dot{\boldsymbol{\theta}}_1, ..., \dot{\boldsymbol{\rho}}_\mathrm{N}, \dot{\boldsymbol{\theta}}_N) \end{aligned} \tag{4}$$

Since we decide to work with the near field dynamics, the translational and rotational kinematics equations become:

$$\mathbf{v}_i = \dot{\boldsymbol{\rho}}_i \tag{5}$$

$$\omega_i = 2\mathbf{G}\left(\mathbf{q}_i\right)\dot{\mathbf{q}}_i \tag{6}$$

where $\mathbf{G}\left(\mathbf{q}_i\right)$ denotes the transformation between angular velocities and rotation parameters. We have:

$$\dot{\mathbf{r}}_i = \dot{\mathbf{R}}_0 + \dot{\boldsymbol{\rho}}_i + \boldsymbol{\Omega} \times \boldsymbol{\rho}_i \tag{7}$$

$$\ddot{\mathbf{r}}_i = \ddot{\mathbf{R}}_0 + \ddot{\boldsymbol{\rho}}_i + \boldsymbol{\Omega} \times \boldsymbol{\Omega} \times \boldsymbol{\rho}_i + 2\boldsymbol{\Omega} \times \dot{\boldsymbol{\rho}}_i \tag{8}$$

We also use the notation

$$\tilde{\omega} = skew(\omega) = \begin{bmatrix} 0 & -\omega_3 & \omega_2 \\ \omega_3 & 0 & -\omega_1 \\ -\omega_2 & \omega_1 & 0 \end{bmatrix} \tag{9}$$

Measuring translational quantities with respect to $\mathcal{F}_{ORF}$,the translational and rotational bus dynamics equations become:

$$m_i\ddot{\boldsymbol{\rho}}_i = -m_i\ddot{\mathbf{R}}_0 - m_i\boldsymbol{\Omega} \times \boldsymbol{\Omega} \times \boldsymbol{\rho}_i - 2m_i\boldsymbol{\Omega} \times \dot{\boldsymbol{\rho}}_i + m_i\mathbf{R}\ddot{\mathbf{r}}_i + \mathbf{f}_e \tag{10}$$

with

$$\ddot{\mathbf{r}}_i = \left(\frac{f_S}{m_i} - \mu_S\right)\frac{\mathbf{r}_i}{\left|\mathbf{r}_i\right|^3} - \mu_E\frac{\left(\mathbf{r}_i - \mathbf{r}_E\right)}{\left|\mathbf{r}_i - \mathbf{r}_E\right|^3} + \mathbf{A}_i\frac{\mathbf{f}_a}{m_i} \tag{11}$$

and

$$\mathbf{J}_i\dot{\boldsymbol{\omega}}_i + \boldsymbol{\omega}_i \times (\mathbf{J}_i\boldsymbol{\omega}_i + \mathbf{h}_i) = \mathbf{r}_{cp2cm} \times f_S \frac{\mathbf{r}_i}{|\mathbf{r}_i|^3} + \boldsymbol{\tau}_a + \boldsymbol{\tau}_e \tag{12}$$

$$\dot{\mathbf{h}}_i = -\boldsymbol{\tau}_a \tag{13}$$

where m_i and $\mathbf{J}_i$ are the mass and moment of inertia matrix of the i-th body, $\mathbf{f}_S$ is the solar force acting on the i-th body, μ_S and μ_E represent the solar and Earth gravitational parameters, $\mathbf{h}_i$ represents the internal angular momentum distribution for the i-th body (originated by reaction wheels), $\mathbf{r}_{cp2cm}$ represents the vector from center of mass to center of pressure of the i-th body, $\mathbf{f}_a$ and $\boldsymbol{\tau}_a$ represent actuator control forces and torques, and $\mathbf{f}_e$ and $\boldsymbol{\tau}_e$ represent the generalized structural reaction forces and moments at the root of each appendage. The combined model of the bus plus appendages is based on eliminating these constraint reaction forces and torques via finite element assembly.

2.1 Disturbances and Actuator Model

The disturbance models that we consider acting on the spacecraft bus are: gravity, solar pressure, and actuator forces and torques. These perturbations are already included in equation (11) and in equation (12). The i-th body is modeled as a rigid cylinder.

Control inputs are reaction wheel forces and torques. For the reaction wheel dynamic model, we adopt a generic wheel model. Three reaction wheels are located and centered along the spacecraft principal axes. Each reaction wheel dynamics is as described in equation (13).

3 CONSTRAINED FLEXIBLE BODY DYNAMICS

Hamilton's Principle states that, for any kinematically admissible variation of the displacement and rotation fields, i.e. allowed by the geometry of the motion, the following stationarity condition holds for a system $\mathcal{S}$ of nb bodies:

$$\sum_{i=1}^{nb} \int_{i}^{i+1} \left[\delta\mathcal{L}\left(\boldsymbol{\eta}, \dot{\boldsymbol{\eta}}, t\right) + \mathcal{F} \cdot \delta\boldsymbol{\eta}\right] dt = \left[\boldsymbol{\sigma} \cdot \delta\boldsymbol{\eta}\right]_i^{i+1} \tag{14}$$

where $\mathcal{L}\left(\boldsymbol{\eta}, \dot{\boldsymbol{\eta}}, t\right) = \mathcal{T}\left(\boldsymbol{\eta}, \dot{\boldsymbol{\eta}}\right) + \mathcal{U}\left(\boldsymbol{\eta}, t\right)$ is the Lagrangean of $\mathcal{S}$, $\mathcal{T}\left(\boldsymbol{\eta}, \dot{\boldsymbol{\eta}}\right)$ is the kinetic energy of $\mathcal{S}$ and $\mathcal{U}\left(\boldsymbol{\eta}, t\right)$ the potential energy of $\mathcal{S}$, $\boldsymbol{\eta}$ and $\dot{\boldsymbol{\eta}}$ are the vectors of generalized coordinates and speeds, $\boldsymbol{\sigma}$ is the vector of generalized momenta, and $\mathcal{F}$ is the vector of generalizes forces. For simplicity, let us impose that $\delta\boldsymbol{\eta} = \mathbf{0}$ at the boundaries of the time interval. The vectors $\boldsymbol{\eta}$, $\dot{\boldsymbol{\eta}}$, and $\mathcal{F}$ are defined as follows:

$$\boldsymbol{\eta} = (\mathbf{r}_i, \mathbf{q}_i) \tag{15}$$

$$\delta\boldsymbol{\eta} = (\delta\mathbf{r}_i, \boldsymbol{\theta}_{\delta i}) \tag{16}$$

$$\dot{\boldsymbol{\eta}} = (\dot{\mathbf{r}}_i, \boldsymbol{\omega}_i) \tag{17}$$

$$\mathcal{F} = (\mathbf{f}_g + \mathbf{f}_i, \boldsymbol{\tau}_i) \tag{18}$$

where $\boldsymbol{\theta}_{\delta i}$ stands for a virtual variation of the quasicoordinate describing the rotation The vectors $\mathbf{f}_i$ and $\boldsymbol{\tau}_i$ include external perturbation and control forces, and $\mathbf{f}_g$ represents the gravitational force $-\mu m_i \frac{\mathbf{r}_i}{|\mathbf{r}_i|^3}$. Therefore $\mathbf{A}_i = \mathbf{A}_i\left(\mathbf{q}_i\right)$. From eq. (14), we obtain

$$\begin{aligned} & \sum_{i=1}^{nb} \delta\mathbf{r}_i \cdot \left(m_i \ddot{\mathbf{r}}_i + \mu m_i \frac{\mathbf{r}_i}{|\mathbf{r}_i|^3} - \mathbf{f}_i \right) + \\ & \boldsymbol{\theta}_{\delta i} \cdot \left(\mathbf{J} \dot{\boldsymbol{\omega}}_i + \tilde{\boldsymbol{\omega}}_i \mathbf{J} \boldsymbol{\omega}_i - \boldsymbol{\tau}_i \right) \\ = \; & 0 \end{aligned} \tag{19}$$

The virtual displacements $\delta\mathbf{r}_i$ and virtual rotations $\boldsymbol{\theta}_{\delta i}$ in eq. (19) are kinematically admissible as they satisfy any constraint equation imposed on body i, namely if

$$\boldsymbol{\Phi}_{\mathbf{r}_i} \cdot \delta\mathbf{r}_i + \boldsymbol{\Phi}_{\theta_i} \cdot \boldsymbol{\theta}_{\delta i} = 0 \tag{20}$$

where $\boldsymbol{\Phi} = \left[\boldsymbol{\Phi}_{\mathbf{r}_i}, \boldsymbol{\Phi}_{\theta_i}\right]$ represents the Jacobian of a certain algebraic equation

$$\Psi = \Psi\left(\eta, \dot{\eta}, t\right) = 0 \tag{21}$$

Therefore, there exists a vector of Lagrange multipliers $\boldsymbol{\lambda}$ such that the new equations of motion become:

$$\begin{aligned} & \sum_{i=1}^{nb} \delta\mathbf{r}_i \cdot \left(m_i \ddot{\mathbf{r}}_i + \mu m_i \frac{\mathbf{r}_i}{|\mathbf{r}_i|^3} - \mathbf{f}_i - \boldsymbol{\Phi}_{\mathbf{r}_i}^T \boldsymbol{\lambda} \right) + \\ & \boldsymbol{\theta}_{\delta i} \cdot \left(\mathbf{J}_i \dot{\boldsymbol{\omega}}_i + \tilde{\boldsymbol{\omega}}_i \mathbf{J}_i \boldsymbol{\omega}_i - \boldsymbol{\tau}_i - \boldsymbol{\Phi}_{\theta_i}^T \boldsymbol{\lambda} \right) = 0 \end{aligned} \tag{22}$$

Finally, for arbitrary admissible $\delta\mathbf{r}_i$ and $\boldsymbol{\theta}_{\delta i}$, we obtain the following equations of motion for body i:

$$m_i \ddot{\mathbf{r}}_i = -\mu m_i \frac{\mathbf{r}_i}{|\mathbf{r}_i|^3} + \mathbf{f}_i + \boldsymbol{\Phi}_{\mathbf{r}_i}^T \boldsymbol{\lambda} \tag{23}$$

$$\mathbf{J}_i \dot{\boldsymbol{\omega}}_i + \tilde{\boldsymbol{\omega}}_i \mathbf{J}_i \boldsymbol{\omega}_i = \boldsymbol{\tau}_i + \boldsymbol{\Phi}_{\theta_i}^T \boldsymbol{\lambda} \tag{24}$$

An alternative, more rigorous derivation invokes a generalized Lagrangean $\mathcal{G}\left(\eta, \dot{\eta}, t\right) = \mathcal{L}\left(\eta, \dot{\eta}, t\right) + \boldsymbol{\Phi}^T \boldsymbol{\lambda}$. The set of equations for body i are eq.(23), eq. (24), and eq. (13).

The equations of motion can now be written in matrix form as:

$$\begin{bmatrix} \mathbf{M} & \boldsymbol{\Phi}^T \\ \boldsymbol{\Phi} & \mathbf{0} \end{bmatrix} \begin{pmatrix} \ddot{\eta} \\ \lambda \end{pmatrix} = \begin{pmatrix} \mathbf{g} \\ 0 \end{pmatrix} \tag{25}$$

where

$$\begin{pmatrix} \ddot{\eta} \\ \lambda \end{pmatrix} = \begin{pmatrix} \ddot{\mathbf{r}}_i \\ \dot{\boldsymbol{\omega}}_i \\ \ddot{\mathbf{r}}_j \\ \dot{\boldsymbol{\omega}}_j \\ \lambda_r \\ \lambda_\theta \end{pmatrix} \tag{26}$$

$$\begin{pmatrix} \mathbf{g} \\ \boldsymbol{\Gamma} \end{pmatrix} = \begin{pmatrix} \mathbf{f}_i - \mu m_i \frac{\mathbf{r}_i}{|\mathbf{r}_i|^3} \\ \boldsymbol{\tau}_i - \tilde{\boldsymbol{\omega}}_i \mathbf{J}_i \boldsymbol{\omega}_i \\ \mathbf{f}_j - \mu m_j \frac{\mathbf{r}_j}{|\mathbf{r}_j|^3} \\ \boldsymbol{\tau}_j - \tilde{\boldsymbol{\omega}}_j \mathbf{J}_j \boldsymbol{\omega}_j \\ 0 \end{pmatrix} \tag{27}$$

$$\mathrm{M} = \begin{bmatrix} m_i\mathbf{1}_3 & 0 & & \\ 0 & \mathbf{J}_i & \multicolumn{2}{c}{\mathbf{0}} \\ \multicolumn{2}{c}{\mathbf{0}} & m_j\mathbf{1}_3 & 0 \\ & & 0 & \mathbf{J}_j \end{bmatrix} \tag{28}$$

$$\mathbf{\Phi} = \begin{bmatrix} \mathbf{\Phi}_{\mathbf{r}_i} & \mathbf{0} & \mathbf{\Phi}_{\mathbf{r}j} & \mathbf{0} \\ \mathbf{0} & \mathbf{\Phi}_{\theta_i} & \mathbf{0} & \mathbf{\Phi}_{\theta j} \end{bmatrix} \tag{29}$$

4 APPENDAGE EQUATIONS

If the appendage was a continuous member (a cantilevered beam, for instance) the equations of motion for each appendage in global coordinates (subscript $_g$)can be written as follows:

$$M_g\ddot{\mathbf{q}} + K_g\mathbf{q} = \mathbf{f}_R \tag{30}$$

where the vector $\mathbf{q}$ (of dimension $n_g \times 1$) contains the nodal displacements and rotations of each node in global coordinates, and $\mathbf{f}_R$ represents the vector of generalized external forces on the appendage nodes.

In our analysis, we noticed that a better correlation with the experimental modal frequencies of each appendage (monopole and dipole booms) can be achieved if the appendage is modeled as a series of elastic Bernoulli-Euler beams connected serially to each other by spherical joints, each joint supporting a rotational spring (in each direction). Instead of the fixed boundary condition at the root, a spherical joint with the root hinge spring constants provided by the TRW report was used. The model of the appendage then becomes:

$$M_t\ddot{\mathbf{q}}_t + K_t\mathbf{q}_t = \mathbf{f}_t \tag{31}$$

where the vector $\mathbf{q}_t$ (of dimension $n_t \times 1$) contains the nodal displacements and rotations of each node in global coordinates, and $\mathbf{f}_t$ represents the vector of generalized external forces on the appendage nodes. Here, n_t is the total number of degrees of freedom of each elastic segment times the number of segments. The model is in block diagonal form as

$$M_t = \begin{bmatrix} M_1 & 0 & \cdots & 0 \\ 0 & M_2 & \cdots & 0 \\ \vdots & \vdots & \ddots & \vdots \\ 0 & 0 & \cdots & M_n \end{bmatrix} \tag{32}$$

$$K_t = \begin{bmatrix} K_{11} & -K_{12} & \cdots & 0 \\ -K^T{}_{12} & K_{22} & \cdots & 0 \\ \vdots & \vdots & \ddots & \vdots \\ 0 & 0 & \cdots & K_n \end{bmatrix} \tag{33}$$

where K_{ij} includes the effect of the rotational spring at the hinge and root.

For an ideal spherical joint, the constraint Jacobian is

$$\mathbf{\Phi} = [\mathbf{\Phi}_{\mathbf{r}_i}, \mathbf{0}, \mathbf{\Phi}_{\mathbf{r}j}, \mathbf{0}] \tag{34}$$

with $\mathbf{\Phi}_{\mathbf{r}_i} = -\mathbf{1}_3$ and $\mathbf{\Phi}_{\mathbf{r}j} = \mathbf{1}_3$.

5 COMPONENT MODEL REDUCTION

In this section, we obtain an expression of the reduced set of multiflexible body dynamics equations.

The algorithm makes use of the Singular Value Decomposition (SVD) to project the equations of motion of the constrained system into the tangent subspace of the motion (eliminates reaction forces and torques between pairs of interacting bodies).

The equations of motion with the constraints may be written as

$$\mathbf{M}\ddot{\eta} + \mathbf{K}\eta + \mathbf{\Phi}_q^T \boldsymbol{\lambda} = \mathbf{G}\mathbf{u} + \mathbf{Q} \tag{35}$$

$$\mathbf{\Phi}_q \dot{\eta} = \nu(\mathbf{t}) \tag{36}$$

$$\mathbf{\Phi}_q \ddot{\eta} = \gamma(\mathbf{t}) \tag{37}$$

By introducing a coordinate transformation $\mathbf{P}$ such that

$$\eta = \mathbf{P}\mathbf{q_r} = \begin{pmatrix} P_1 & P_2 \end{pmatrix} \begin{pmatrix} \mathbf{q}_{r1} & \mathbf{q}_{r2} \end{pmatrix}^T \tag{38}$$

where

$$\mathbf{P}_{1[n\times m]} = \mathbf{orth}\left(\mathbf{\Phi}_q^T\right) \tag{39}$$

and

$$\mathbf{P}_{2[n\times (n-m)]} = \mathbf{null}\left(\mathbf{\Phi}_q\right) \tag{40}$$

one obtains a projection of the dynamics of the constrained system in a direction tangent to the *constraint manifold*. The matrix $\mathbf{P}$ maps the minimal system state $\mathbf{q}_r$ into the global system state η. This means that the projected system moves in the direction of the kinematically admissible displacements, and the effect of the constraints on the balance of forces vanishes. This transformation is equivalent to the one obtained via a singular value decomposition of the constraint jacobian, i.e.:

$$[P, \Sigma, V] = \mathbf{svd}\left(\mathbf{\Phi}_q^T\right) \tag{41}$$

such that

$$\mathbf{\Phi}_q \mathbf{P}_1 \text{ is invertible} \tag{42}$$

$$\mathbf{P}_2^T \mathbf{\Phi}_q^T = 0 \tag{43}$$

Therefore, by premultiplying the equations of motion of each appendage by $\mathbf{P}_2$, we have a way to eliminate the reaction forces from the equations of motion. This elimination process is exact, however it requires some extra computation at each integration time since the algebraic operations required by the SVD may be time consuming. This is a marginal problem, since this computation is carried out off-line, before the dynamic simulation is carried out. Inserting eq.(38) into the equations of motion eq.(35), we obtain:

$$\mathbf{P}_2^T \mathbf{M} \mathbf{P}_2 \ddot{\mathbf{q}}_r + \mathbf{P}_2^T \mathbf{K} \mathbf{P}_2 \mathbf{q}_r + \boxed{\mathbf{P}_2^T \mathbf{\Phi}_q^T \boldsymbol{\lambda}} = \mathbf{P}_2^T \mathbf{G}\mathbf{u} + \mathbf{P}_2^T \mathbf{Q} \tag{44}$$

where the enclosed term vanishes because of equation (43).

The reduced model of the appendage then becomes:

$$M_r \ddot{\mathbf{q}}_r + K_r \mathbf{q}_r = \mathbf{P}_2^T \mathbf{G}\mathbf{u} + \mathbf{P}_2^T \mathbf{Q} = \mathbf{f}_r \tag{45}$$

where the vector $\mathbf{q}_r$ (of dimension $n_r \times 1$) contains the reduced nodal displacements and rotations of each node in global coordinates, and $\mathbf{f}_r$ represents the vector of generalized external forces on the appendage nodes.

6 COUPLING THE BUS EQUATIONS WITH THE APPENDAGE MULTIBODY EQUATIONS

The wheel can be seen as a freely rotating body which is coupled to the base structure via a revolute joint. Assume that there exists a finite element model of the base structure. The wheel can be modeled with a localized inertia at a particular node, where the degree of freedom corresponding to the wheel rotation is left free. The equations of motion of the rigid spacecraft bus (superscript 1) and of node w (location of reaction wheel) are as follows:

$$\begin{aligned} M^1_{bus}\ddot{\mathbf{d}} + S^1_{bus}\dot{\boldsymbol{\omega}} &= \mathbf{f}^i && (46)\\ S^i_{bus}\ddot{\mathbf{d}} + J^i_{bus+w}\dot{\boldsymbol{\omega}} + J^w_w\dot{\boldsymbol{\Omega}} + G^i(\mathcal{H}^w)\boldsymbol{\omega} + \boldsymbol{\omega} \times (J^i_{bus+w}\dot{\boldsymbol{\omega}}) &= \boldsymbol{\tau}^i - \boldsymbol{\tau}^w_w && (47)\\ J^w_w\dot{\boldsymbol{\omega}} + J^w_w\dot{\boldsymbol{\Omega}} &= \boldsymbol{\tau}^w_w && (48) \end{aligned}$$

where $\mathbf{d}$ is the nodal displacement, $\boldsymbol{\omega}$ is the nodal angular velocity, and $\boldsymbol{\Omega}$ is the wheel rate vector, ${\boldsymbol{\tau}_{\mathbf{w}}}^w$ is the vector of reaction wheel actuation torque, $\mathbf{f}^i$ is the vector of external forces at node i, and $\boldsymbol{\tau}^i$ is the vector of external torques at node i. M^i_{bus} is the mass matrix of node i, S^i_{bus} the first moment of inertia matrix, J^i_{bus+w} the second moment of inertia matrix, J^w_w the diagonal matrix of wheel axial inertia, and $G^i(\mathcal{H}^w)$ is the skew-symmetric gyroscopic matrix, which depends on the relative angular momentum $\mathcal{H}^w$ present at node w.

The equations of motion for the spacecraft in global coordinates (subscript $_g$)can be written as follows:

$$M_g\ddot{\mathbf{q}} + (G_g + D_g)\dot{\mathbf{q}} + K_g\mathbf{q} = \mathbf{u}$$

where the vector $\mathbf{q}$ (of dimension $n_g + 1 \times 1$) contains the nodal displacements and rotations of each node in global coordinates plus the reaction wheel rotation angles plus the degrees of freedom of the bus, and $\mathbf{u}$ is the vector of nodal external forces and moments (including external perturbations and control forces and moments) on the bus node, and the reaction wheel torques. Some nodes are artificially defined to be the optics nodes, and they do not have any mass or stiffness properties associated with them. Hence, the global equations need to be reduced from the global set n_g to a set of independent degrees of freedom n_e. This is done by the transformation $\mathbf{q} = T\mathbf{q_e}$, where T is of dimension $n_g \times n_e$.

Splitting the equations in elastic (e) and rigid (r) coordinates, we have:

$$\begin{aligned} M_{ee}\ddot{\mathbf{q}}_e + M_{er}\dot{\boldsymbol{\Omega}} + (G_{ee} + D_{ee})\dot{\mathbf{q}}_e + K_{ee}\mathbf{q}_e &= f_e && (49)\\ M_{re}\ddot{\mathbf{q}}_e + M_{rr}\dot{\boldsymbol{\Omega}} &= f_r && (50) \end{aligned}$$

where now $M_{ee} = T^T M_g T$, and so on. With the assumptions stated above, i.e., by assuming small angular rates (so that the nonlinear terms are negligible, and the modes are still the mass-normalized undamped modes), we can impose the modal transformation $\mathbf{q}_e = \phi\eta$, and rewrite the equations as:

$$\begin{aligned} \ddot{\eta} + \{\phi^T[G(\mathcal{H}^w)]\phi + 2\Lambda\xi\}\dot{\eta} + \Lambda^2\eta + \phi^T M_{er}\dot{\boldsymbol{\Omega}} &= \phi^T T^T b\mathbf{f_r} && (51)\\ M_{re}\phi\ddot{\eta} + M_{rr}\dot{\boldsymbol{\Omega}} &= \mathbf{f_r} && (52) \end{aligned}$$

where ϕ is the modal matrix, Λ is the diagonal matrix of natural frequencies, and ξ is the modal damping coefficient. We assume some percentage of modal damping in the computations. Clearly, $M_{rr} = J^w_w$, $M_{re} = {M_{er}}^T$ is the coupling inertia term, and $\mathbf{f_r}$ is the vector of the wheel disturbance forces and torques on the bus, plus the reaction wheel actuation torques.

Introducing the state vector as $\mathbf{x} = (\eta, \beta, \dot{\eta}, \Omega)^T$, where β represents the reaction wheel angle, the state space model becomes as follows:

$$\begin{aligned} \dot{\mathbf{x}} &= A\mathbf{x} + B\mathbf{u} && (53) \\ \mathbf{y} &= C\mathbf{x}+D\mathbf{u} && (54) \end{aligned}$$

where $\mathbf{u}$ is the vector of inputs (reaction wheel torque at location w), and is the observation matrix which reads all the finite element state vector. The state matrices are as follows:

$$A = \begin{bmatrix} \mathbf{0} & \mathbf{I} \\ -M^{-1}K & -M^{-1}(G+D) \end{bmatrix} \tag{55}$$

$$M = \begin{bmatrix} \mathbf{I} & \phi^T M_{er} \\ M_{er}\phi & M_{rr} \end{bmatrix} \tag{56}$$

$$K = \begin{bmatrix} \mathbf{K}_{ee} & \mathbf{0} \\ \mathbf{0} & \mathbf{0} \end{bmatrix} \tag{57}$$

$$G + D = \begin{bmatrix} \phi^T[G(\mathcal{H}^w)]\phi + 2\Lambda\xi & \mathbf{0} \\ \mathbf{0} & \mathbf{0} \end{bmatrix} \tag{58}$$

$$B = \begin{bmatrix} \mathbf{0} \\ -\phi^T T^T b \\ \mathbf{0} \quad \mathbf{I}_{3x3} \end{bmatrix} \tag{59}$$

$$b = \begin{bmatrix} \mathbf{0} & \mathbf{I}_{3\times3} & -\mathbf{I}_{3\times3} \end{bmatrix} \tag{60}$$

$$C = \begin{bmatrix} T\phi & 0 & 0 & 0 \\ 0 & \mathbf{I} & 0 & 0 \\ 0 & 0 & T\phi & 0 \\ 0 & 0 & 0 & \mathbf{I} \end{bmatrix} \tag{61}$$

7 EIGENSPECTRUM

The eigenspectrum of the whole vehicle, including the rigid rotors is shown in Figure 3, while the eigenspectrum of the dipole and monopole booms is shown in Figure 4 and Figure 5, respectively. The comparison with the experimental data reported in the JPL Memorandum (Ref. [2]) is excellent.

8 CONTROL LAWS

The control laws applied to the spacecraft are of the feedback (proportional-derivative) plus feed-forward type. The translation control actually implemented on the spacecraft is of the form

$$\mathbf{f} = K_p(\mathbf{s}_{Cmd} - \mathbf{s}_{Est}) + K_v(\dot{\mathbf{s}}_{Cmd} - \dot{\mathbf{s}}_{Est}) + M^i\ddot{\mathbf{s}}_{Cmd} \tag{62}$$

where $\mathbf{s}$ represents the position vector of the center of mass, K_p and K_v are translation control gain matrices, M is the spacecraft mass matrix, q_{Est} and q_{Cmd} represent the estimated and commanded translation state, respectively. The rotational control instead is of the following form

$$\boldsymbol{\tau} = \Gamma_p(\boldsymbol{\lambda\theta}_{err}) + \Gamma_v(\boldsymbol{\omega}_{Cmd} - \boldsymbol{\omega}_{Est}) + J\ddot{\boldsymbol{\alpha}}_{Cmd} \tag{63}$$

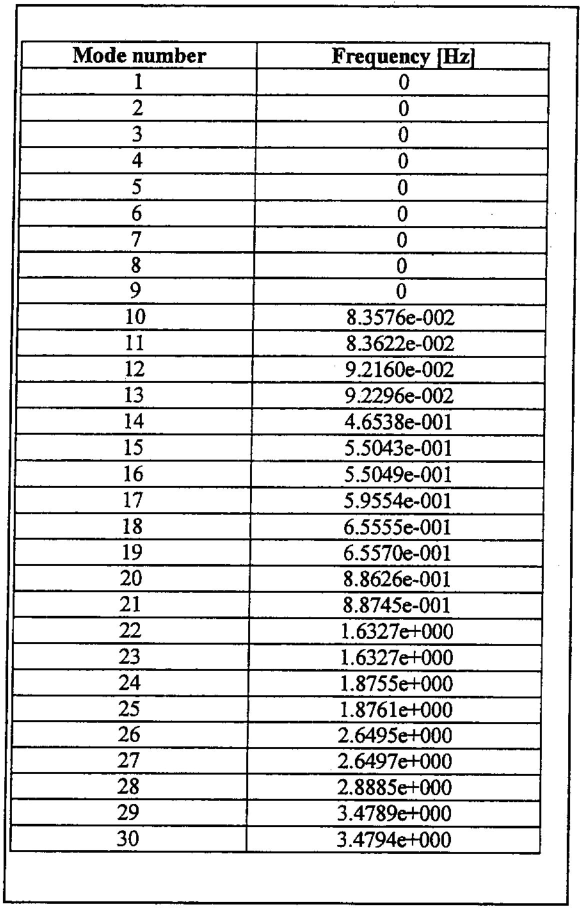

Mode number	Frequency [Hz]
1	0
2	0
3	0
4	0
5	0
6	0
7	0
8	0
9	0
10	8.3576e-002
11	8.3622e-002
12	9.2160e-002
13	9.2296e-002
14	4.6538e-001
15	5.5043e-001
16	5.5049e-001
17	5.9554e-001
18	6.5555e-001
19	6.5570e-001
20	8.8626e-001
21	8.8745e-001
22	1.6327e+000
23	1.6327e+000
24	1.8755e+000
25	1.8761e+000
26	2.6495e+000
27	2.6497e+000
28	2.8885e+000
29	3.4789e+000
30	3.4794e+000

Figure 3: Frequencies of MARSIS vehicle dynamics.

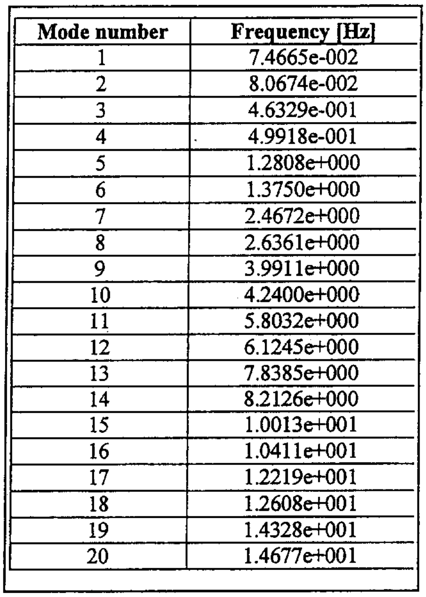

Mode number	Frequency [Hz]
1	7.4665e-002
2	8.0674e-002
3	4.6329e-001
4	4.9918e-001
5	1.2808e+000
6	1.3750e+000
7	2.4672e+000
8	2.6361e+000
9	3.9911e+000
10	4.2400e+000
11	5.8032e+000
12	6.1245e+000
13	7.8385e+000
14	8.2126e+000
15	1.0013e+001
16	1.0411e+001
17	1.2219e+001
18	1.2608e+001
19	1.4328e+001
20	1.4677e+001

Figure 4: Frequencies of Dipole Boom.

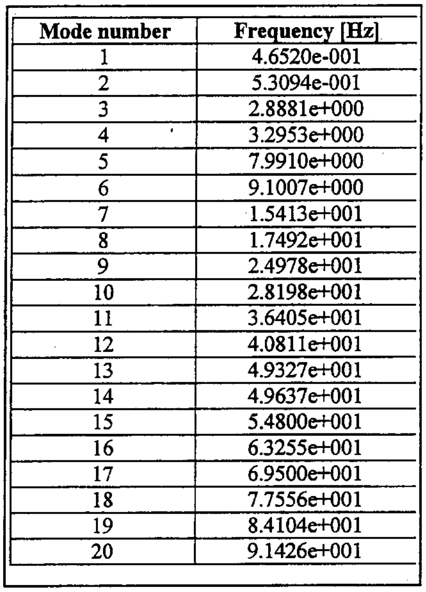

Mode number	Frequency [Hz]
1	4.6520e-001
2	5.3094e-001
3	2.8881e+000
4	3.2953e+000
5	7.9910e+000
6	9.1007e+000
7	1.5413e+001
8	1.7492e+001
9	2.4978e+001
10	2.8198e+001
11	3.6405e+001
12	4.0811e+001
13	4.9327e+001
14	4.9637e+001
15	5.4800e+001
16	6.3255e+001
17	6.9500e+001
18	7.7556e+001
19	8.4104e+001
20	9.1426e+001

Figure 5: Frequencies of Monopole Boom.

where Γ_p and Γ_v are rotational control gain matrices, J is the spacecraft moment of inertia matrix, λ is the eigenaxis of rotation, and θ_{err} is the magnitude of rotation corresponding to the difference between the commanded and the estimated quaternions.

As per equation (13), the torques in equation (63) are applied with negative sign to the reaction wheels. The control gains were chosen as follows:

direction	proportional gain [Nm/rad]	derivative gain [Nms/rad]
roll	1.7028e2	3.9582e+2
yaw	1.7028e2	3.9582e+2
pitch	4.7300e1	1.0995e2

On account of the closed reaction wheel loops, the eigenstructure for a model with 4 modes becomes as follows:

mode	open loop pole [Hz]	closed loop pole [Hz]
1	0	0
2	0	0
3	0	0
4	0	0
5	0	0
6	0	0
7	0	5.9197e-2
8	0	8.3560e-2
9	0	8.3605e-2
10	8.3560e-2	9.2141e-2
11	8.3605e-2	9.2277e-2
12	9.2141e-2	1.4400e+0
13	9.2277e-2	4.2351e+0

Figures 6, 8, 7, and 9 show transfer functions from pitch reaction wheel torque to bus center of mass displacement, velocity, angles, and angle rates.

9 NUMERICAL SIMULATION

A numerical simulation has been carried out to show the performance of the model. The spacecraft bus is given an excitation by a reaction wheel torque pulse of 0.33Nm for a duration of 6 second about the bus Z-axis (pitch). Axes X (roll) and Y (yaw) are not actuated. A closed loop proportional-derivative controller from spacecraft angles and angular rates to spacecraft body torques is applied to maintain the monopole antenna and Y axis always pointed along the Nadir direction (local Mars vertical). Figure 10 depicts the torque profile applied to the pitch axis, designed to excite the 0.083 Hz mode. Figures 11, 12, and 13 depict the open loop response of the system (roll, yaw, and pitch angle) to the torque input with 2% damping. Figure 14 shows the effect of 2% and 5% damping on the yaw rate. Figures 15, 17, 19, and Figures 16, 18, 20, show the roll, yaw, and pitch angles of the bus with 5% and, respectively, 2% structural damping is applied to the monopole and dipole booms.

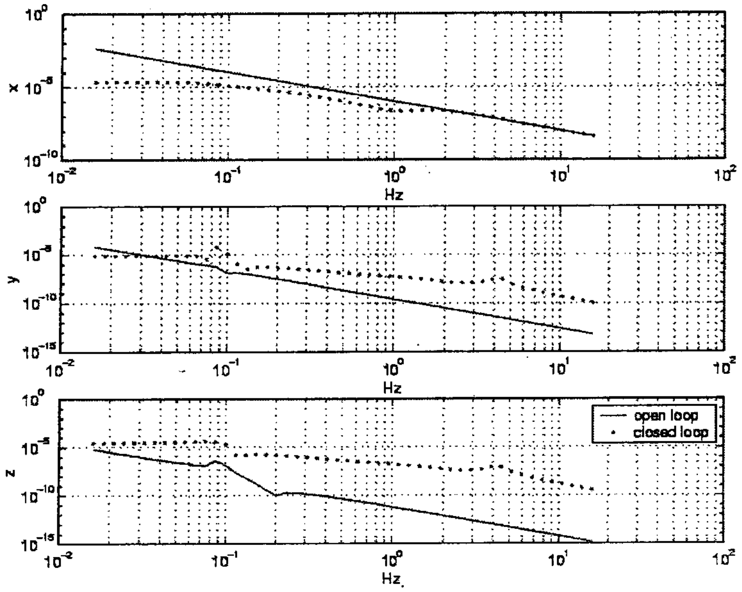

Figure 6: Bode plots of transfer functions from pitch reaction wheel input to X, Y, Z bus center of mass displacements.

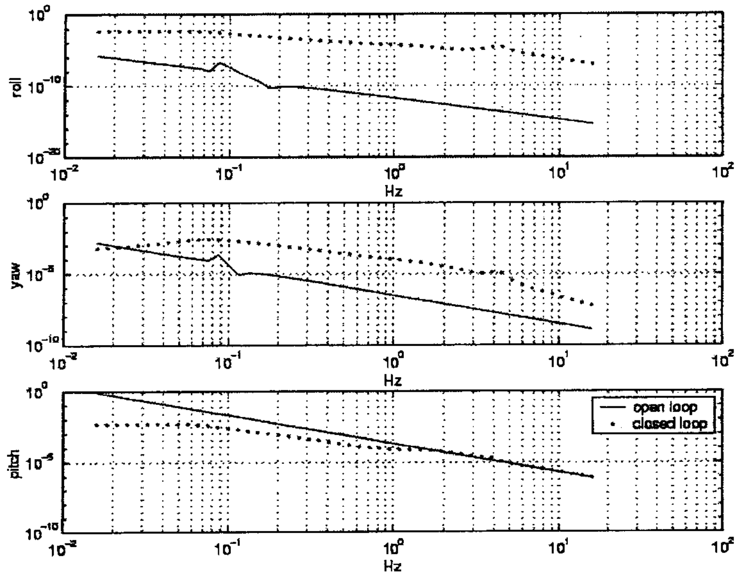

Figure 7: Bode plots of transfer functions from pitch reaction wheel input torque to bus roll, yaw, and pitch angles.

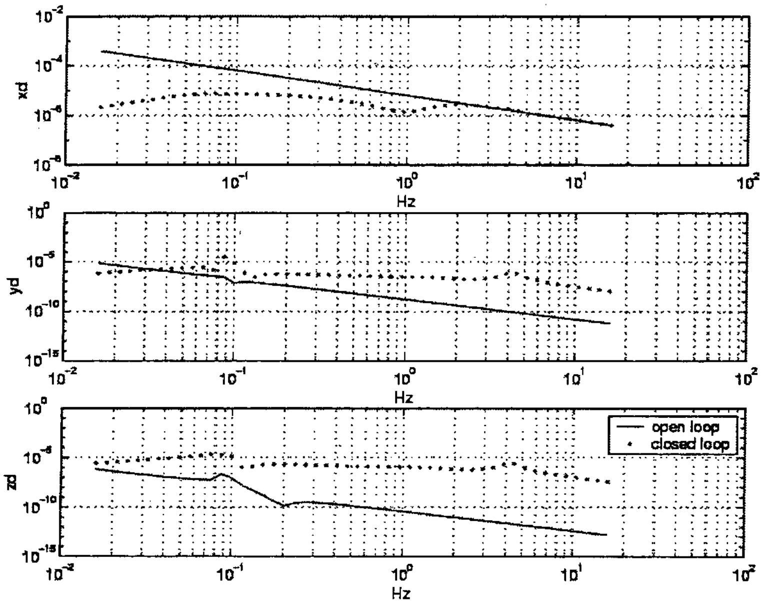

Figure 8: Bode plots of transfer functions from pitch reaction wheel input to X, Y, Z bus center of mass velocities.

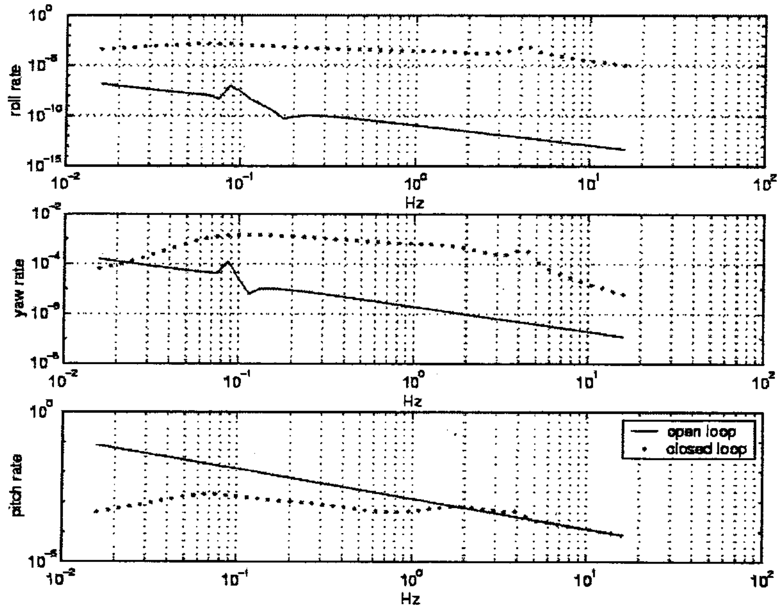

Figure 9: Bode plots of transfer functions from pitch reaction wheel input torque to bus roll, yaw, and pitch rate.

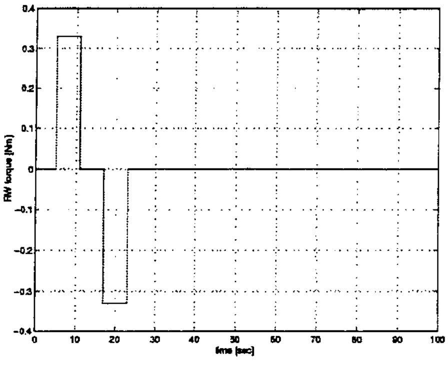

Figure 10: Applied pitch reaction wheel torque vs. time.

A significant increase in residual oscillations results when a lower level of damping is present, as it is to be expected. Finally, Figure 21 shows the pitch axis reaction wheel speed during the transient maneuver, in which approximately 475 rpm are reached (the spin inertia of each wheel is 0.2 kgm^2), for a change in angular momentum of 1.66 Nms. The maximum momentum storage capability of each reaction wheel is 10 Nms.

With the Reaction Wheel control loops closed, the disturbed response of the spacecraft bus to a Pitch axis symmetric torque pulse waveform of +/-2 Nms (+/-0.33 Nm for 6 seconds) was settled within 10 seconds following the end of the symmetric input disturbance. This disturbance torque profile was deliberately designed to excite the 20 m boom fundamental mode of 0.0835 Hz (measured with the attitude loops open) and also have a net zero momentum transfer to the bus and zero steady state rate. The residual settling oscillations after 10 seconds had amplitudes of sub-arcseconds with a frequency of 0.125 Hz. The residual oscillations had damping decrements of 40 seconds for 50% peak amplitude decay with the 5% structural damping factor, and 55 seconds with the 2% damping factor. The peak bus motion for both dampings was +/- 0.2 degrees in pitch motion. Apparently, the Reaction Wheel closed loop damping of the disturbed bus was far more effective in controlling its settling motion than the structural damping. This is as it should be for such low frequency appendage dynamics.

10 CONCLUSIONS

As predicted from boundary condition theory for cantilevered beams, the resulting open-loop oscillatory dynamics of the spacecraft central body are significantly (~12%) higher in frequency (0.0835 Hz) then the individual 20-meter boom modal dynamics of 0.0746 Hz. Two levels (2% and 5%) of boom structural damping were used in the simulations. Following the imposed disturbance, the open-loop settling time with 2% damping to a peak-peak oscillation of ~0.002 degrees was ~77 seconds. Importantly, with the attitude control system (ACS) Reaction Wheels in a closed-loop mode, the corresponding settling time to sub-arcsecond stability in the local-vertical local-horizontal Mars centered frame was very short (~10 seconds). With the system in a closed-loop mode, the effective inertial stiffness was increased and the bus settling oscillation frequency was about 50% higher at 0.125 Hz compared to the open-loop condition. From this analysis we can conclude that the MARSIS booms have open-loop dynamic properties compatible with the Mars Express Spacecraft. Further-

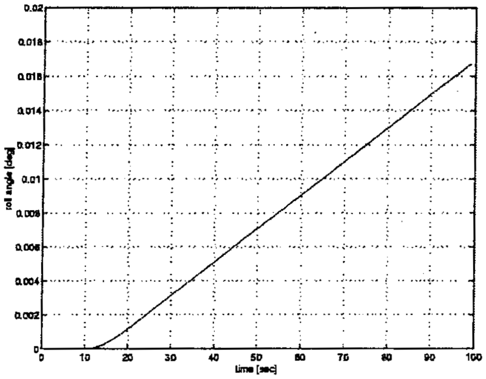

Figure 11: Roll angle vs. time with no feedback (2% damping).

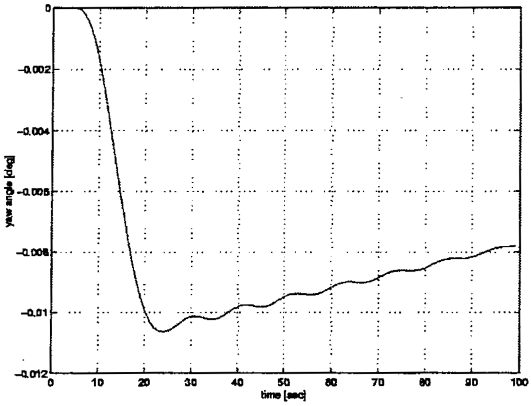

Figure 12: Yaw angle vs. time with no feedback (2% damping).

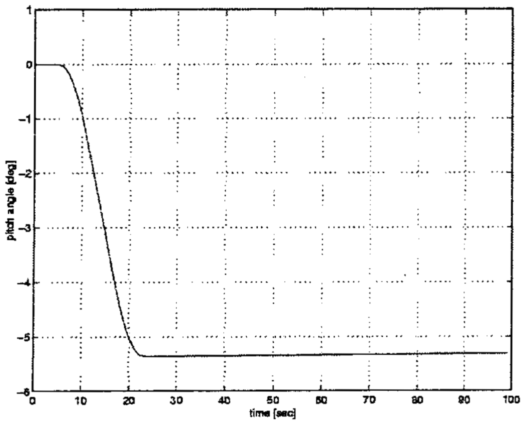

Figure 13: Pitch angle vs. time with no feedback (2% damping).

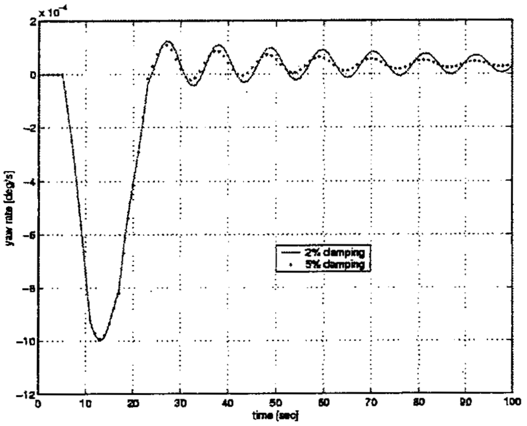

Figure 14: Yaw rate vs. time with no feedback.

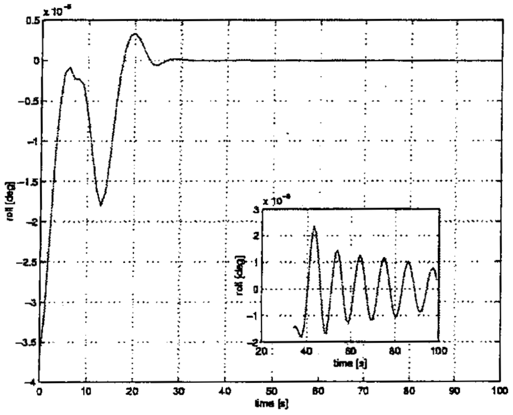

Figure 15: Roll angle with 5% damping and feedback.

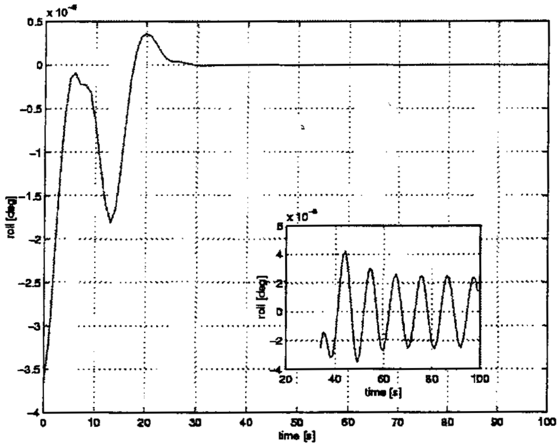

Figure 16: Roll angle with 2% damping and feedback.

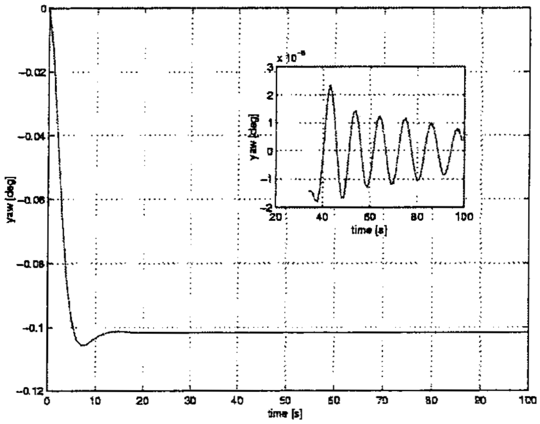

Figure 17: Yaw angle with 5% damping and feedback.

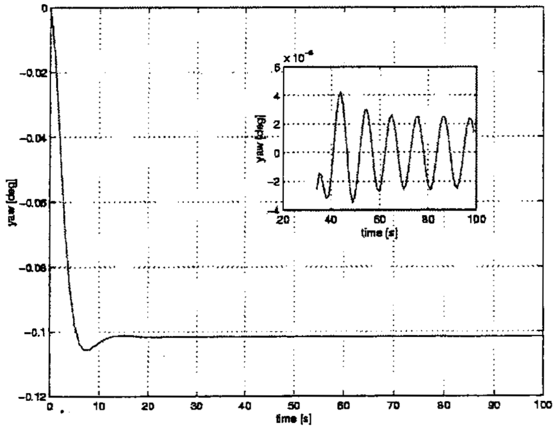

Figure 18: Yaw angle with 2% damping and feedback.

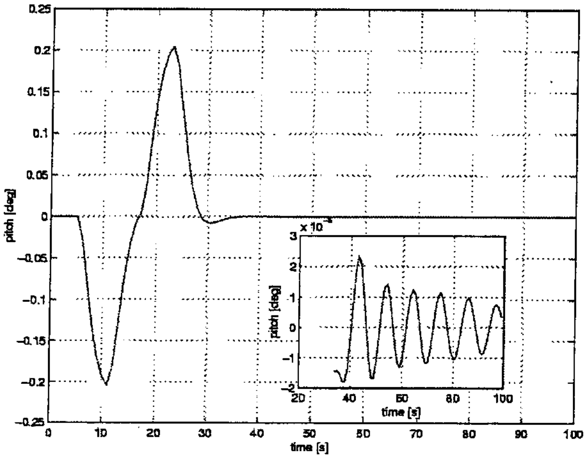

Figure 19: Pitch angle with 5% damping and feedback.

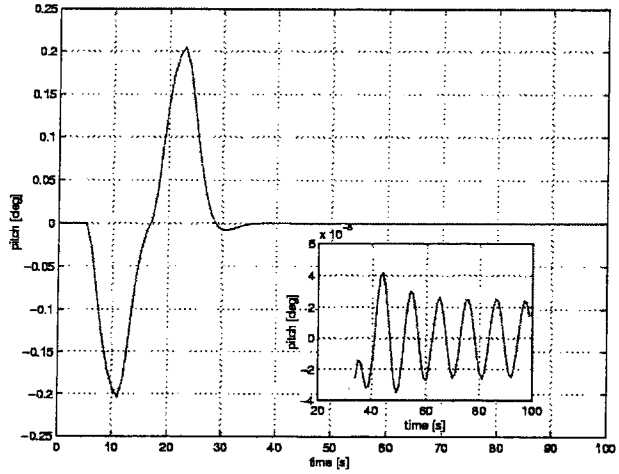

Figure 20: Pitch angle with 2% damping and feedback.

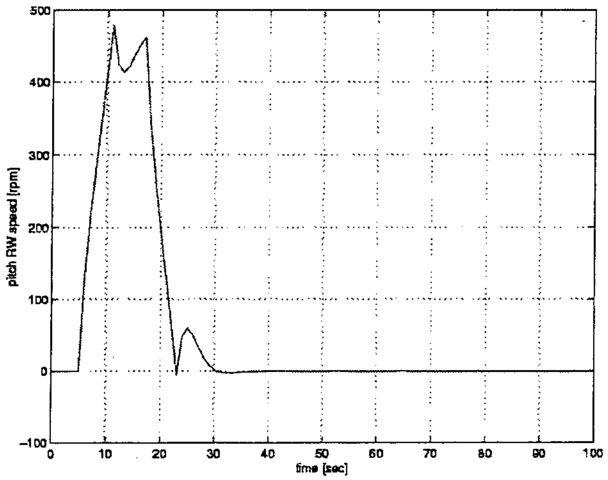

Figure 21: Pitch Reaction Wheel speed in rpm during maneuver with feedback.

more, we can predict that a realistically sized Reaction Wheel Controller will be able to suppress the antenna residual transient vibration dynamics so that it contributes negligible error to the mission science pointing accuracy and jitter (line-of-sight stability) capabilities.

Acknowledgements: The research described in this paper was carried out at the Jet Propulsion Laboratory, California Institute of Technology, under a contract with the National Aeronautics and Space Administration. The authors wish to gratefully acknowledge the detailed technical information expeditiously provided by personnel at TRW Astro Aerospace, Goleta and Carpenteria, CA, and with the Mars Express Project at Astrium, Toulouse, France. We also wish to extend our appreciation to the JPL MARSIS Experiment project managers who encouraged our independent examination of the design, modeling, and testing of the antenna booms to establish the highest confidence in its deployment and in-flight dynamics compatibility with the Mars Express mission. Finally, we wish to acknowledge our JPL colleague, Jeff Umland, for his helpful technical discussions.

References

[1] TRW Astro Aerospace Memorandum, April 2, 2002.

[2] Umland J. and Mettler E., *MARSIS Antenna Element Frequency Estimate Review Findings*, JPL Interoffice Memorandum 352B-JWU-02-IOM, February 25, 2002.

[3] Harris, C.M. editor: *Shock and Vibration Handbook*, 4th Edition, Chapter 7, McGraw Hill, 1996.

[4] Mettler, E. and Quadrelli, M., *Modeling and Analysis of MARSIS Boom Dynamics*, JPL Engineering Memorandum 3457-02-005, and JPL Document D-23738, May 6, 2002